Applied Surface Science 604 (2022) 154585

Contents lists available at ScienceDirect

Applied Surface Science

journal homepage: www.elsevier.com/locate/apsusc

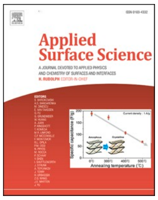

Full Length Article

A universal substrate for the nanoscale investigation of two-dimensional materials

Tuan-Hoang Tran [a], Raul D. Rodriguez [a,*], Dmitry Cheshev [a], Nelson E. Villa [a], Muhammad Awais Aslam [b], Jelena Pešić [c], Aleksandar Matković [b], Evgeniya Sheremet [a]

[a] Tomsk Polytechnic University, Lenina ave. 30, Tomsk, Russia
[b] Institute of Physics, Montanuniversität Leoben, Franz Josef Strasse 18, 8700 Leoben, Austria
[c] Institute of Physics Belgrade, University of Belgrade, Pregrevica 118, 11080 Belgrade, Serbia

ARTICLE INFO

Keywords:
Highly-oriented pyrolytic graphite
Graphene substrate
2D materials
Straintronics
Nanoscale characterization

ABSTRACT

Since discovering two-dimensional materials, there has been a great interest in exploring, understanding, and taking advantage of their unique properties. Si/SiO$_2$ is one of the most used substrates for the deposition and characterization of 2D materials due to its availability and optical contrast. This work goes beyond the conventional substrate and introduces highly-ordered pyrolytic graphite (HOPG) as universal support for investigating two-dimensional materials due to several unique properties such as chemical and temperature stability, intrinsic high flatness, reusability, electrical conductivity, ease of use, availability, and enhanced adhesion of two-dimensional materials. We demonstrate this by analyzing several 2D materials with advanced atomic force microscopy methods, Raman and photoluminescence spectroscopy with hyperspectral imaging, and scanning electron microscopy with elementary analysis imaging. The strong adhesion to HOPG allowed the instant deposition of different two-dimensional materials GaSe, MoS$_2$, Zn$_2$In$_2$S$_5$, talc, and h-BN. This feat is hard to accomplish on the conventional SiO$_2$ substrate without polymer-assisted transfer. Moreover, this strong interaction can strain 2D materials deposited on HOPG, giving localized changes in reactivity, optical, and electronic properties. This effect is explored for selective Ag deposition on strained regions of 2D materials to activate photocatalytic reactions.

1. Introduction

Two-dimensional (2D) nanomaterials keep on attracting great interest thanks to their remarkable electrical, optical, mechanical, and chemical properties, exploitable in diverse applications [1]. Their studies shot up thanks to analytical methods that allowed us to investigate the intrinsic properties of 2D materials [2]. Most studies have used insulating materials such as h-BN and Si/SiO$_2$ as default substrates. Thanks to its flatness, chemical stability, optical properties, and relatively low cost, Si/SiO$_2$ is beneficial for several analytical methods [3,4]. However, the surface of the commonly used Si/SiO$_2$ substrates involves many configurations due to its amorphous nature with possible both O-polar and Si-polar defects. The surfaces with uncontrolled or unwanted defects strongly affect the electronic properties of 2D materials. To avoid this, SiO$_2$ is H-passivated to minimize the effects on the electronic properties of the 2D materials deposited on top, [5] or passivated *via* self-assembled hydrophobic monolayers, as hexamethyldisilazane [6]. Its electrically insulating nature makes the 2D electron gas decouple from the surroundings, allowing to study of the intrinsic properties of 2D materials. On the other hand, this makes conventional insulating substrates inconvenient for nanoscale electrical characterization methods such as Kelvin probe force microscopy (KPFM), conductive atomic force microscopy (C-AFM), and scanning electron microscopy (SEM).

Gold is also a choice; however, gold has to be evaporated on flat substrates such as glass, mica, or silicon, where adhesion layers such as Ti, Cr, or Pt have to be used, limiting reusability. Moreover, gold surfaces must be annealed to obtain crystalline flat planes, which are also limited to a smaller lateral size of 100 nm [7]. Compared to Au and Si/SiO$_2$ substrates, a freshly cleaved highly-oriented pyrolytic graphite (HOPG) surface obtained by mechanical exfoliation is the flattest, cleanest and easiest support for 2D materials one could get. Furthermore, HOPG has an excellent electrical conductivity that allows studying the electrical properties of conductors, semiconductors, and insulators at the nanometer scale. Due to the van der Waals force, we

---

* Corresponding author.
E-mail address: raul@tpu.ru (R.D. Rodriguez).

https://doi.org/10.1016/j.apsusc.2022.154585
Received 24 June 2022; Received in revised form 13 August 2022; Accepted 16 August 2022

expect that 2D materials will strongly couple to HOPG, forming vdW heterostructures that allow us to investigate such systems' novel properties [8]. This expectation of heterostructures' formation is justified by density functional theory (DFT) calculations in previous studies for various 2D materials combined with graphene [9,10].

Previous works showed HOPG as a substrate for synthesizing and studying nanostructures [11,12]. Those studies were motivated by HOPG chemical and temperature stability critical to synthesis processes. For example, HOPG benefits as a substrate were shown by the electrodeposition of various chalcogenides, especially on graphite steps, [13] or by investigating structural and local electronic properties of WS_2/WSe_2 heterostructures [14].

Thus, there seems to be an untapped potential in HOPG that could allow the systematic study of physical, chemical, electrical, and structural properties using the same van der Waals support typical for 2D material heterostructures. We investigated this possibility by atomic force microscopy (AFM)-based methods, including scanning capacitance microscopy (SCM), KPFM, and IV-curves at the nanoscale. HOPG as a substrate allowed us to obtain optical and structural properties of different 2D layers by photoluminescence (PL) and Raman microspectroscopy. Without spectral overlap between 2D materials and the substrate, these analyses were possible since, except for the shear mode of multilayer graphene, HOPG does not have any Raman modes in the frequency range of most 2D materials (10–600 cm^{-1}). In addition, the excellent thermal conductivity of HOPG helps with heat dissipation, preventing burning or modifying heat-sensitive materials. The surface morphology and elemental content were investigated by SEM and energy dispersive X-ray (EDX) spectroscopy without resorting to deposition of a conductive coating that would be otherwise required with insulating substrates. Our results are not limited to a single 2D material, but we demonstrate its universality by investigating different layered systems mechanically exfoliated from bulk crystals. Our results show not only the nanoscale analysis of a widely-studied 2D material like MoS_2 or its well-known cousin GaSe, but we also report for the first time a new 2D material never investigated before in its 2D nanosheet van der Waals form, $Zn_2In_2S_5$ (ZIS). Surprisingly, we found that the strong interaction

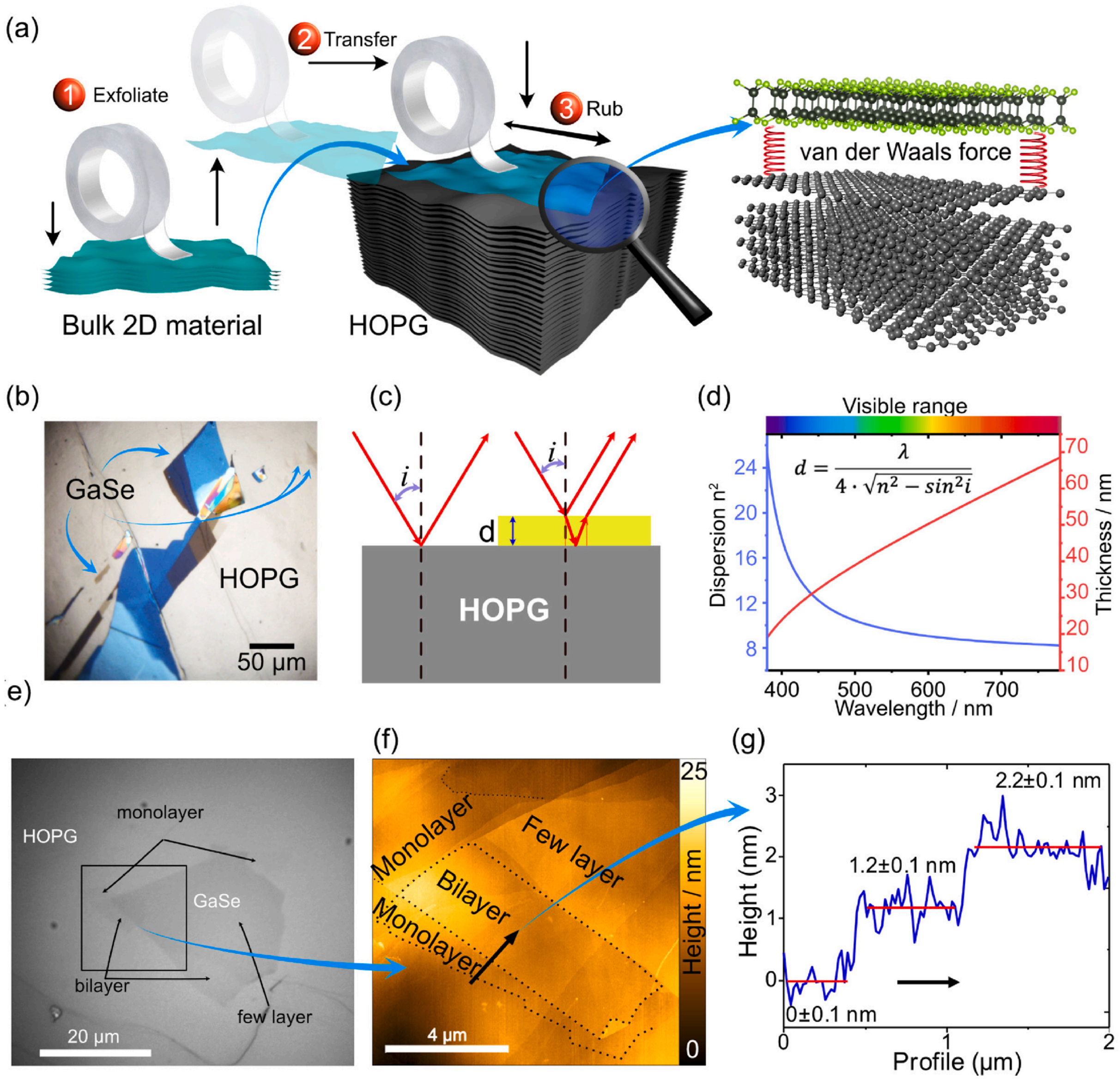

Fig. 1. a) Deposition of 2D materials on HOPG, b) Optical image of GaSe layers with different thicknesses on HOPG. c) Optical interference schematics showing the optical paths in the system of 2D materials on HOPG. d) A plot of refractive index dispersion dependence on wavelength and GaSe thickness according to the interference maxima wavelength for zero order. e) Optical image of the region of interest with a 100x objective shown in brown color scheme for improved contrast. f) AFM topography of GaSe. g) Cross-section profile showing thicknesses corresponding to bilayer and monolayer GaSe.

between the 2D materials and HOPG leads to complete imprinting of the substrate's structural defects on the 2D layer deposited on top. Consequently, the 2D material properties could be tuned by pre-patterning or pre-straining/wrinkling the HOPG substrate [15]. Finally, we illustrate this application with the modification of GaSe on HOPG, showing the change in optical, electronic, and catalytic properties due to the strong surface/2D material interaction as a proposal to straintronics.

2. Results and discussion

2.1. Contaminant-free direct deposition of 2D materials and layer thickness determination by optical contrast

Polydimethylsiloxane (PDMS) is often used to transfer 2D layers to different substrates with the so-called dry transfer method or PDMS stamp method [16]. Despite its convenience that allows transfer to arbitrary substrates, this method is prone to sample contamination by PDMS residues affecting the characterization results [17]. Therefore, we wondered if HOPG could help develop a transfer method for 2D materials that is PDMS residue-free, inexpensive, fast, and easy to implement. We investigated the 2D material deposition directly on HOPG with the hypothesis that a strong interaction between the two materials makes the instant deposition of 2D layers possible. We verified this hypothesis by touching the HOPG surface with different layered crystals (see Video S1 in the Supporting Information and Fig. 1**a**). In a matter of seconds, we obtained a large number of thin layers deposited over an extended area without adhesive tape or other transfer residual contamination (see Fig. 1**b and 1e**). The many different colors are due to light interference in the layers with different thicknesses, as schematically presented in Fig. 1**c**. This feature allows us to estimate the flake thickness from an optical microscopy image alone. The interference maximum is given by $m\lambda = 2d\sqrt{n^2 - sin^2 i} - \frac{\lambda}{2}$, where d – flake thickness, n – refractive index, i– angle of incidence, and m – order of interference maximum. Considering that $m = 0$ and $i = 22^\circ$ (half of beam convergence angle), the 2D layer thickness can be defined as $d = \frac{\lambda}{4\sqrt{n^2 - sin^2 i}}$. The dispersion equation for GaSe was defined by Kato *et al.* and expressed as $n^2 = 10.6409 + \frac{0.3788}{\lambda^2 - 0.1232} + \frac{7090.7}{\lambda^2 - 2216.3}$ [18]. Fig. 1**d** shows the dependence on the wavelength that defines the flake color as a function of layer thickness. We notice that the objective has a set of angles. It leads to a small error (±0.4 nm) in the thickness calculation.

For ultrathin sub-10 nm layers, the interference condition set by equation (1) obviously cannot be achieved for visible light; instead, we observe these layers in grayish color. Realizing this point allows us to quickly inspect and select those ultrathin layers for which remarkable properties are often observed.

This visual observation can be explained by optical contrast. For instance, Li *et al.* used the optical contrast to identify 1L — 15L ultrathin 2D layers made of graphene, MoS_2, WSe_2, and TaS_2 on 90 and 300 nm Si/SiO_2 [19]. Complex reflectivity defines the effect of substrate, with low substrate reflectivity generally giving a high contrast [20]. This is why 2D layers and graphene are so hard to see on highly reflective surfaces like Au or Ni [21]. The optical contrast of 2D materials on a substrate depends on the number of layers, numerical aperture of the objective, wavelength, and optical properties of the layer and the substrate [22]. Contrary to HOPG, the optical contrast of 2D materials on Si/SiO_2 has been studied extensively [22,23]. Thanks to the low substrate reflectivity, graphene is readily visible on Si/SiO_2 with an optimal thickness of 90 or 280 nm enhanced with green filters or without filters under white light illumination [24]. For MoS_2 monolayers, the optimal thickness of SiO_2 is 55 or 220 nm [4]. Interestingly, the optical contrast of 2D materials on HOPG has not been investigated so far. We expected that because of its low reflectance of 0.26804 at 587.6 nm, which is approximately equal to that of Si/SiO_2 [25]. This is an exciting and valuable result since we can still visualize ultrathin layers despite the lack of optical interference in HOPG.

Fig. 1**e** shows a visual image of GaSe flakes on HOPG with the dark brown color observed under a 100x microscope objective with a halogen lamp and objective NA = 0.7. AFM imaging results of the gray region in Fig. 1**f** show that these are ultrathin GaSe layers with thickness down to 2.2 nm and 1.2 nm (see Fig. 1**e**), which correspond to bilayer and monolayer GaSe, respectively [26]. In addition, MoS_2 monolayer was also visually observed on HOPG, as discussed later on. Herein, we perform a layer thickness *vs* optical contrast evaluation that shows the possibility for fast characterization of the 2D material thickness using HOPG as a substrate. The optical contrast (OC) is defined $OC = 1 - \frac{R_{2dm+Sub}}{R_{sub}}$, where $R_{2dm+Sub}$ and R_{sub} are the reflection intensity from 2D material on the substrate and bare substrate, respectively. The OC for monolayer and bilayer GaSe was calculated as 3 ± 1 % and 8.0 ± 1 %, respectively.

Optical and AFM topography images were also obtained for h-BN and talc, showing the HOPG universality for 2D materials deposition and optical observation from multilayer to ultrathin (see **Figure S1** in Supporting Information). Thus, HOPG as a substrate allows the quick identification of ultrathin 2D layers that appear grayish under a conventional optical microscope.

2.2. Electronic characterization of two-dimensional layers on HOPG substrates with KPFM and SCM

Since Nonnenmacher *et al.* first introduced Kelvin probe force microscopy (KPFM) in 1991, [27] KPFM has become more and more popular in the electronic characterization of semiconductor, metal, organic, and 2D material devices [28,29]. In KPFM, as shown in Fig. 2**a and 2b**, the sample is grounded, and a direct (DC) potential is applied at the tip to nullify the first harmonic electrostatic force $F_\omega = \frac{dC}{dz}(V_{DC} - V_{CPD})V_{AC}sin(\omega t)$, where V_{DC} and V_{CPD} are direct potential and contact potential difference (CPD) between the tip and sample, respectively.

Therefore, KPFM allows evaluating the work function of materials since under these conditions $V_{CPD} = \frac{\Phi_{tip} - \Phi_{sample}}{e}$, where Φ_{tip} and Φ_{sample} are the work functions of tip and sample, respectively, and e is the electronic charge [30]. When the two materials are not connected, their vacuum levels are aligned, but their Fermi levels differ. When electrically connecting both materials, the Fermi levels align by charge flow between the two materials (see Fig. 2**b**). After both materials become charged, an electrostatic force arises between the tip and the sample. In KPFM, this force is nullified by applying an external DC voltage that matches the contact potential difference. GaSe is one of the 2D group-III metal monochalcogenides and has been used in nonlinear optical applications [31]. The electronic properties of 2D materials strongly depend on the number of layers. For instance, bulk GaSe has a bandgap of 2.1 eV, while monolayer GaSe is predicted to have a bandgap of 3.5 eV [32]. Therefore, knowing the work function of GaSe flakes for different layer thicknesses is essential so that appropriate metals can be chosen to tune the band alignment and design devices with desired properties. The AFM topographies of monolayer, trilayer, and bulk GaSe, along with their height profiles, are presented in Fig. 2**c**. The thickness of the GaSe monolayer is (1.2 ± 0.2) nm, in excellent agreement with values reported in the literature [26,33]. The corresponding KPFM surface potential map is shown in Fig. 2**d**. HOPG domains in the CPD image are related to water and hydrocarbon adsorption on twisted graphene in HOPG [34]. Interestingly, the CPD of bulk GaSe with a thickness of 42.5 nm is (29.8 ± 0.5) mV. The CPD of GaSe decreases when decreasing layer thickness from (−36.5 ± 0.4) mV to (−51 ± 0.5) mV for trilayer and monolayer GaSe, respectively. A PtIr-coated AFM tip (Fermi level 4.83 eV) was used to measure the sample's CPD, which allowed us to deduce that the GaSe work function increases from 4.8 eV for the bulk (42.5 ± 0.3 nm layer) to 4.88 ± 0.01 eV for trilayer and monolayer. These values are significantly different from Chong and coauthors' work, [35] who reported that the GaSe work function increases from

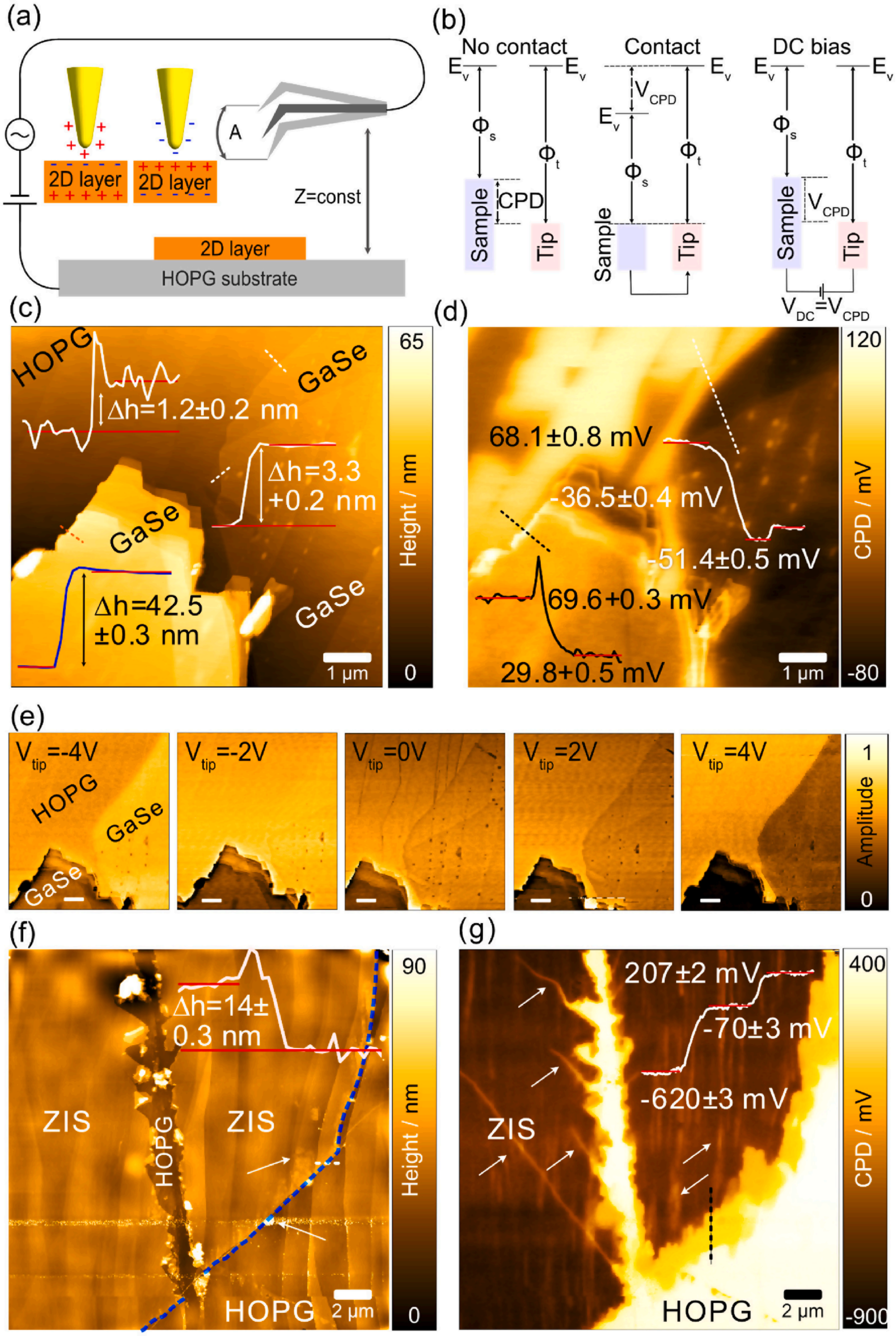

Fig. 2. a) General schematic of KPFM and SCM modes measurement setup. b) KPFM energy diagram. c) AFM topography image of GaSe on HOPG (inset - height profile). d) CPD image of GaSe on HOPG (inset - CPD profile). e) SCM imaging GaSe layers at different applied DC voltages; the scale bar is 2 μm. f) AFM topography image of $Zn_2In_2Z_5$ on HOPG (inset - height profile). The blue-dashed line shows the ZIS/HOPG interface. g) CPD image of ZIS. White arrows show contamination, inset - CPD profile. (For interpretation of the references to color in this figure legend, the reader is referred to the web version of this article.)

4.35 eV to 4.51 eV when the thickness decreases from 15 to 4 layers and then increases to 4.7 eV but for a higher number of layers up to 38. However, in that work, the authors measured samples on a Si/SiO_2 substrate without an external electrical contact that leads to sample charging. In such a case, the CPD becomes more sensitive to surface dipoles and charging effects than the work function.

Controlling the electronic properties of semiconductors and their doping level made possible the technological revolution brought by microelectronics [36]. Further progress is being made by shrinking device dimensions and exploring the potential of 2D materials in nanoelectronics [37]. In this context, we used scanning capacitance microscopy (SCM) to study the charge carrier distribution in a GaSe flake. This was possible thanks to the excellent electrical conductivity of HOPG that provides an opportunity to perform electrical measurements of 2D semiconductors and distinguish them on a well-defined flat background showing only typical terraces of HOPG. Fig. 2**a** shows a simple scheme of the SCM working principle. The sample's topography is recorded in the first pass. Then, in SCM, the tip is lifted by 10 nm in a second scan pass while the tip-sample electrostatic force is recorded at the second harmonic under a potential bias $F_{2\omega} = -\frac{1}{4}\frac{dC}{dz}V_{AC}^{2}sin(2\omega t)$. In this experiment, it is easy to see the difference in capacitance between the 2D sample and the substrate (see Fig. 2**e**). The SCM amplitude signal is related to the local conductivity of the sample, and thus, to the charge carrier mobility and charge carrier density [38]. Regions with bright and dark contrast correspond to high and low conductivity, respectively. The metal-like conductivity of HOPG allows it to be used as a reference to identify n- or p-type regions in the 2D material placed on top. This is the first time that n- or p-type identification has been conducted on a HOPG substrate since mainly Si/SiO$_2$ was employed before for this purpose which can be inaccurate due to surface charging [39,40]. The SCM results at different biases in Fig. 2**e** show that the local conductivity of GaSe decreases as the applied DC voltage to the tip changes from − 4 V to 4 V. While the negative bias voltage induces the accumulation of holes on the surface, the positive bias voltage produces an accumulation of electrons, leading to a low dielectric response. This behavior arises from the p-type conductivity of GaSe [35]. Interestingly, at $V_{DC} = -4$ V, the local conductivity of monolayer and trilayer GaSe is even higher than the local conductivity of HOPG. We attribute this result to the higher hole concentration of p-type GaSe/HOPG than HOPG due to hole doping induced on graphene by GaSe [41].

At − 4 V bias, the local conductivity of GaSe decreases as its thickness decreases due to quantum confinement [42]. We can see that the conductivity of monolayer GaSe is considerably higher than trilayer GaSe at $V_{DC} = -4$ V. However, when $V_{DC} = 4$ V, we do not see differences in charge concentration and mobility of monolayer and trilayer GaSe because of charge carriers' depletion. In addition, the charge carrier density and mobility of a few-layered GaSe is still higher than in bulk GaSe at a bias voltage of 4 V. This result is somewhat unexpected considering that monolayer and few-layer GaSe readily oxidize in air a short time after exfoliation[33,43] so that we expect to see oxidized GaSe with decreased conductivity. High conductivity could occur if oxygen incorporation increases charge carrier density, like in indium tin oxide [44]. Another possibility is that previous reports on the oxidation of GaSe in air are based mainly on Raman spectroscopy. Despite the low laser power used in those reports to avoid oxidation, the laser exposure of GaSe could still induce photooxidation [33,43]. Since our ultrathin GaSe layers were not exposed to laser light during or before our KPFM experiments, we suspect their stability is higher than previously reported. Besides, a bottom graphene layer on SiO$_2$ significantly reduces the degradation of GaTe layers deposited on top due to the hydrophobic nature of graphene [45]. We are now closely looking into this question and plan to report our findings in a separate work.

The changes in electronic properties due to substrate-induced defects by HOPG on GaSe were also investigated by KPFM and SCM. The optical microscopy image and a sketch of the structure are shown in **Figures S2a and S2b**. The AFM topography of GaSe on HOPG defects is shown in **Figure S2c**. The GaSe layer thickness is 6.9 ± 0.2 nm, and the height difference on the step of HOPG is 216.7 ± 0.3 nm (see the profile in **Figures S2d and S2e**). Despite the large step defect size, the thin GaSe flake follows the HOPG topography perfectly. KPFM, SCM, and phase images are presented in **Figures S2f, S2g, and S2h**. The CPD contrast shows that the charge concentration in GaSe is higher in the regions over the HOPG step defect than on the flat HOPG. Moreover, these steps also change the mechanical properties of GaSe as we see the difference of GaSe on the defects and flat HOPG in the phase image in **Figure S2h**.

$Zn_2In_2S_5$ is a novel 2D material with applications such as photocatalysis in nanoparticle form [46]. However, ZIS has not been investigated in the large-scale highly crystalline 2D-layered form, like graphene or MoS$_2$ mechanically exfoliated from bulk crystals. Nevertheless, there is an interesting report by Zhang *et al.* [47] who obtained ZIS nanolayers with sub-micrometer lateral dimensions and showed excellent photocatalytic performance against other zinc sulfide indium phases ($Zn_mIn_2S_{m+3}$, m = 1–3).

Beyond the sample topography information provided by conventional AFM, with its 3D mapping capabilities at the nanoscale, we chose KPFM analysis as a complementary method to map the electronic properties of ZIS on HOPG. The topography image in Fig. 2**f** shows defects and edges of HOPG that are visible through the 14 nm thick $Zn_2In_2S_5$ layer placed on top. The strong van der Waals force between $Zn_2In_2S_5$ and HOPG deforms $Zn_2In_2S_5$ and makes it follow the HOPG topography. This remarkable observation is highly significant since straintronic applications could be developed by first patterning HOPG and then depositing the 2D nanomaterial to mimic the pre-patterned substrate developing predefined strained regions [48]. This way of indirect patterning a 2D material was never attempted before with HOPG and may offer a high-quality crystalline lattice engineering due to the non-invasive approach for introducing strain.

Motivated by the strong adhesion force between 2D material and HOPG, we tested the robustness of this interaction by using force lithography that is remarkably demanding on the 2D material/substrate adhesion. During scratching, a sharp needle effectively removed part of $Zn_2In_2S_5$ and created cracks on the surface visible in the topography image Fig. 2**f**. Making such a mechanically-induced scratch is challenging when using Si/SiO$_2$ wafers as supports since the 2D material just gets dragged over the substrate or folded over the edge due to the strong indenter-sample shear force and weaker 2D/SiO$_2$ adhesion [49]. Fig. 2**g** shows the sample's CPD image (with a CPD value of (−207 ± 2) mV for HOPG), where a similar contrast is observed all over $Zn_2In_2S_5$ except for the regions at the edges and mechanically induced defects. The work function of HOPG is calculated at (4.633 ± 0.002) eV. Due to airborne contamination when measuring in the air, this value is 20 meV higher than in previous reports [34,50]. From the value of $Zn_2In_2S_5$′s CPD of (620 ± 3) mV, we can evaluate the work function of $Zn_2In_2S_5$, at (5.460 ± 0.003) eV. Around the edge on the right side (see the arrow in Fig. 2**f**), the regions with lower CPD are more prominent than around the defects and cracks. The areas with low CPD coincide with the ZIS layer edge at the HOPG interface. The contrast in these regions is due to debris and contaminants observed in the topographic image (Fig. 2**f**). Being able to spatially control the reactivity, surface potential, and surface affinity of 2D materials by lithography is of significant value for nanoelectronics. The KPFM results show that defects propagating from the scratch and defects induced by the substrate have lower CPD than non-defective terraces. Thus, it seems promising to use defects on the HOPG substrate to tune the properties of the 2D material on top as a sort of indirect lithography.

2.3. *Photoluminescence and Raman imaging of MoS$_2$*

The chemical purity and stability of HOPG in contact with multilayered and two-dimensional materials enable conducting micro-Raman spectroscopy, photoluminescence spectroscopy, and other optical and structural analyses of 2D materials without background signals. This is important because no other Raman modes or emission peaks will arise in HOPG since it remains stable during the spectroscopic analysis. Background-free spectroscopy is possible since there is no spectral overlap between the high-frequency G and 2D modes of HOPG substrate with the low-frequency modes of most 2D materials in the spectral range < 600 cm^{-1}. Photoluminescence (PL) and Raman spectroscopies are widely used to detect monolayers of 2D materials and other effects such as doping, strain, temperature, and compositional changes [51,52]. Much attention has been given to the optical properties of MoS$_2$ that we use as a layered model system here. MoS$_2$ was exfoliated and transferred to HOPG by the PDMS transfer method, demonstrating the compatibility of HOPG with this widespread transfer method. The sample consists of a monolayer, few-layer, and bulk MoS$_2$. The sample's topography and phase images are shown in Fig. 3a and 3b. We can distinguish MoS$_2$, HOPG, and PDMS residues on HOPG. The phase contrast from PDMS-transfer residues is higher than that of HOPG and MoS$_2$, related to the higher tip-sample adhesion force for the transfer residues. It is precisely

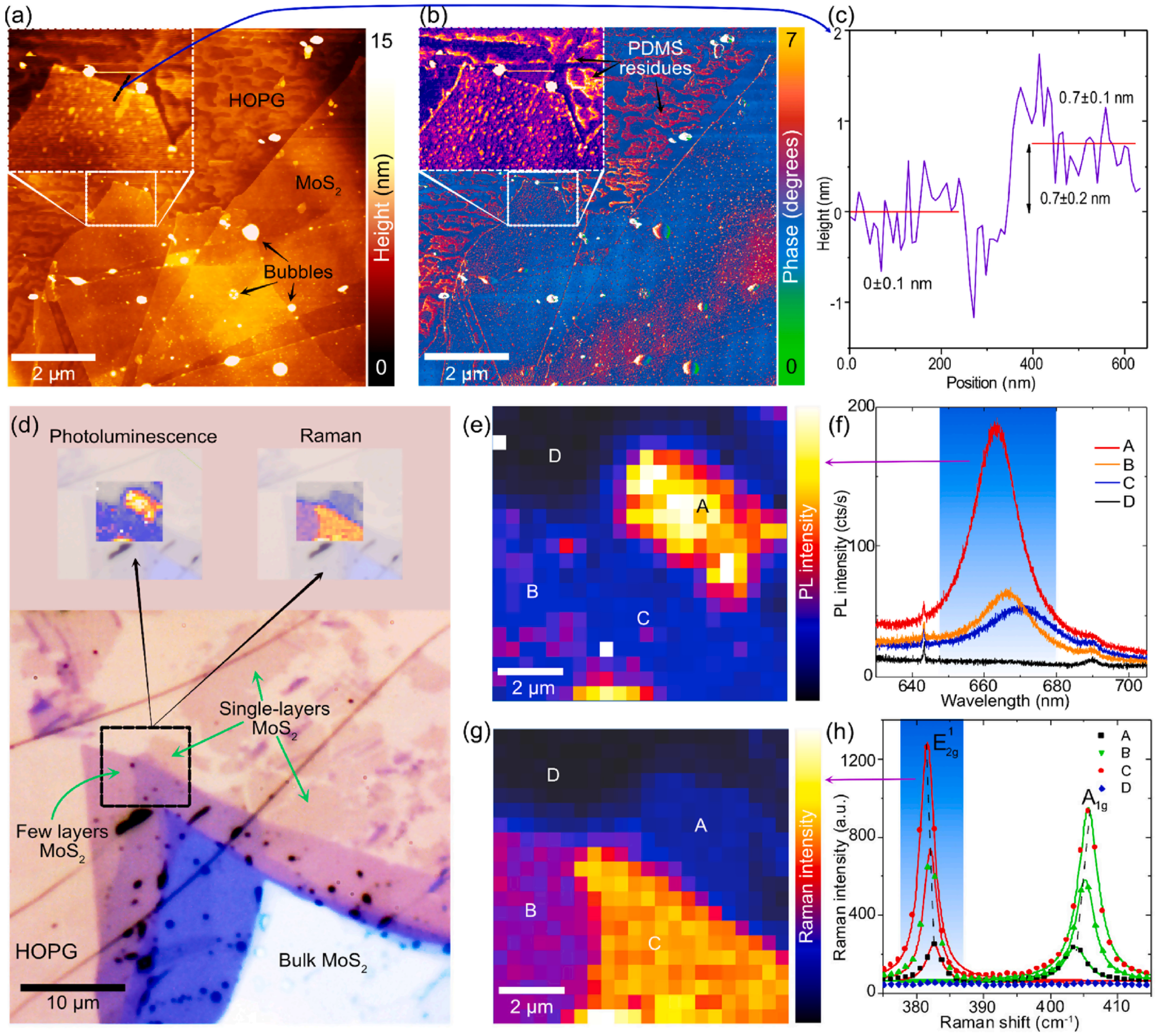

Fig. 3. PL and Raman maps of MoS$_2$ on HOPG. a) AFM topography and b) phase images. c) Single-layer height profile of the regions visible in d) the optical microscopy image. The red lines are linear fits for the substrate and MoS$_2$ monolayer profile with the fitting errors. e) PL map with regions of interest labeled: A-monolayer MoS$_2$, B-bilayer MoS$_2$, C-trilayer MoS$_2$, and D-HOPG. f) PL spectra from different regions of interest. g) Raman intensity map. h) Raman spectra from different regions. (For interpretation of the references to color in this figure legend, the reader is referred to the web version of this article.)

this kind of sample contamination that our rubbing method on HOPG entirely avoids using PDMS or adhesive tape (see Fig. 1 and Fig. 2). In addition to leaving residues, PDMS transfer produces micro-and nano-bubbles on MoS$_2$ [53,54]. These bubbles can be easily noticed in topography and phase images (see Fig. 3**a and 3b**). Despite the residues on HOPG, the 0.7 nm monolayer thickness was determined by the cross-sectional analysis presented in Fig. 3**c** [55,56]. The uncertainties were determined from the linear fits in the cross-sections; we can see that the uncertainties in height profile when using PDMS are more significant than the height value deduced when using our method. From the optical image in Fig. 3**d**, we again see how easy it is to identify 2D monolayers on HOPG despite the absence of optical interference contrary to Si/SiO$_2$.

Fig. 3**e and 3f** show the photoluminescence map and spectra at different sample points: A - monolayer MoS$_2$, B - bilayer MoS$_2$, C - trilayer MoS$_2$, D - HOPG. Monolayer MoS$_2$ shows the strongest PL signal due to the indirect to direct bandgap transition. The PL signal decreases with the increase in the number of MoS$_2$ layers following the literature [55–57]. The PL spectra of few-layer MoS$_2$ on SiO$_2$ substrates exhibit two prominent peaks around 627 and 670 nm [55]. In our system, the second peak is located at 663 nm for the monolayer and shows redshift as the number of layers increases (Fig. 3**f**). This behavior can be related to the strong van der Waals interaction between MoS$_2$ and HOPG. Although the first prominent PL peak of MoS$_2$ coincides with the 2D Raman peak of HOPG at the laser wavelength we used, this overlap could be avoided by changing the laser wavelength.

The Raman map and spectra of a few-layer MoS$_2$ are shown in Fig. 3**g and 3 h**, respectively, perfectly matching previous reports with the E^1_{2g} and A_{1g} phonons around 380 and 400 cm^{-1}, and a prominent peak at approximately 450 cm^{-1} [56]. For monolayer MoS$_2$, the E^1_{2g} mode at 382.6 cm^{-1} has a blue shift compared to monolayer MoS$_2$ measured on SiO$_2$; we attribute this shift to the strong interaction with the substrate. The peak intensity and position show a monotonous change with the number of MoS$_2$ layers. The intensity of all peaks increases when increasing the MoS$_2$ thickness; the E^1_{2g} Raman mode is blue-shifted while the A_{1g} mode shows the expected redshift. Besides the peak shift differences between MoS$_2$ on HOPG and SiO$_2$, these results demonstrate the versatility of HOPG as a substrate for optical spectroscopic analysis of 2D materials. This clean spectroscopic background was critical to acquiring the Raman spectra of talc (10 nm thick) on HOPG in addition to the heat-dissipating, inert, and high adhesion HOPG nature [58].

2.4. Stretching out 2Ds: Straintronics - a multistep defect on HOPG activates the chemical reactivity of a GaSe layer

In recent years, the design of 2D materials has been flourishing thanks to advances in the fundamental understanding of these nanomaterials at the atomic scale. The catalytic activity of materials depends on the number of active sites on the surface [59]. The active sites are defined by their electronic properties on the surface, which can be increased by structural modifications such as surface microstructure. One emerging strategy for structural modification is strain engineering, which allows controlling interfacial charge transfer, surface reactivity, and electronic and photonic performance [60]. Strain can be induced purposely or accidentally like nanolayers over HOPG graphite steps. Stress causes changes in the 2D system, such as increased interatomic distances that make atomic bonding surfaces softer. Moreover, electronic properties also change. For instance, as recently summarized by

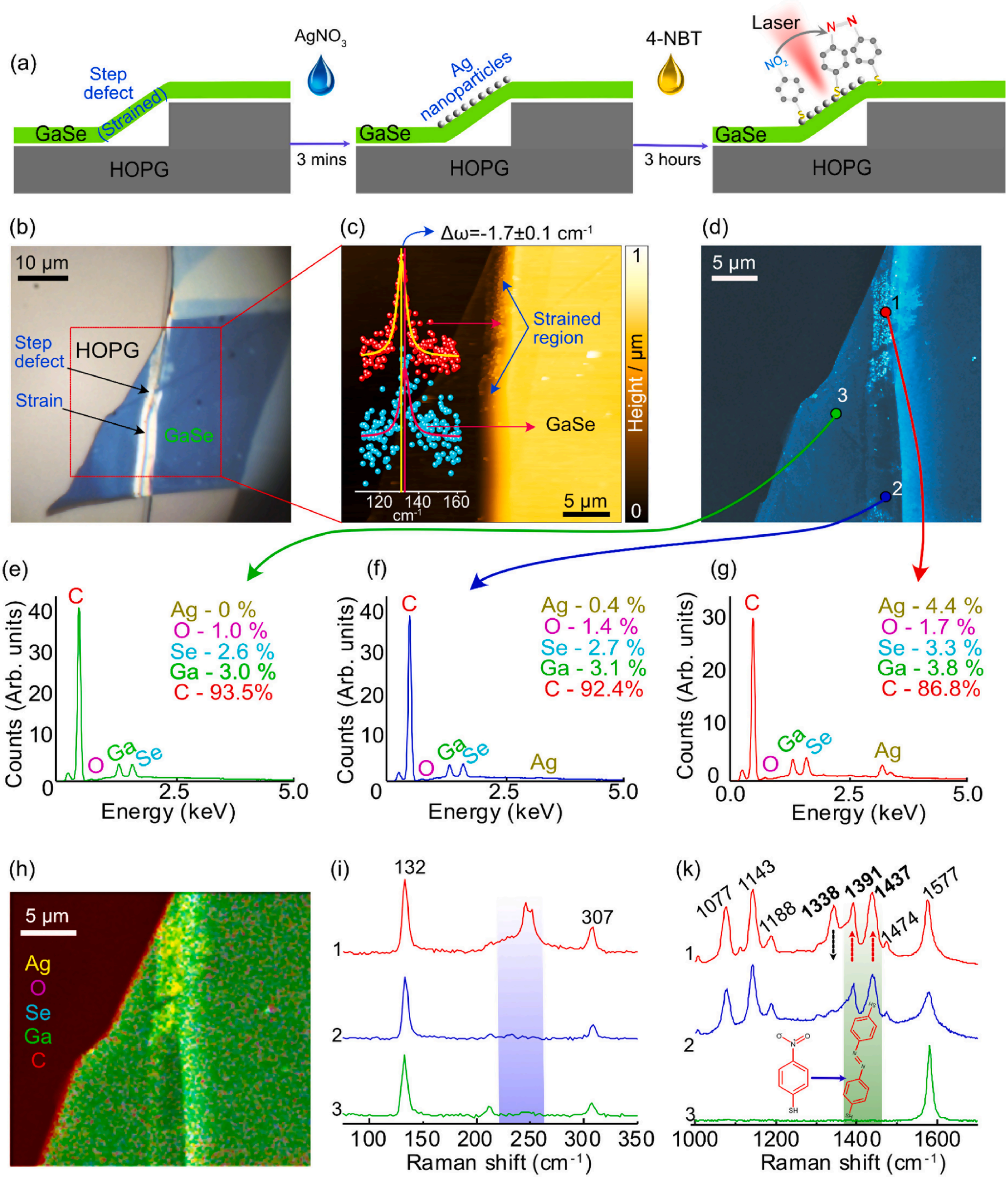

Fig. 4. a) Experimental scheme representing the process of AgNO$_3$ solution deposition, Ag nanoparticles formation, and functionalization with 4-NBT, b) Optical image of GaSe on HOPG after modification by AgNO3, c) AFM and d) SEM images of the region of interest. The inset in c shows the Raman spectra with a down-shift of the A’1 peak for the strained region. (e-g) EDX spectra represent non-strained region e), strained region f), and strained region with Ag nanoparticles. h) Elemental map obtained by EDX. i) Raman spectra of the sample after modification by AgNO3. k) Raman spectra of the sample at different locations after exposure to 4-NBT for 3 h.

Wu *et al.*, charge carriers' concentration, band gap, and phonon modes all get affected by strain [61]. We show in this section that the strong interaction between the 2D material and the HOPG substrate can be exploited to enhance the catalytic activity of GaSe radically. A sketch of the experiment is shown in Fig. 4**a**.

Fig. 4**b** shows the optical microscopy image of a GaSe flake on a step defect of HOPG, showing color changes from blue to light yellow. We anticipated that these translocated defects go beyond modifying the optical properties of the GaSe layer, but its catalytic properties should also be affected. To test this hypothesis, we dropped 10 μL of $AgNO_3$ 10^{-4} M on the sample shown in Fig. 4**b** and let it react for 3 mins. Afterward, $AgNO_3$ was removed and the sample was washed several times with distilled water to remove $AgNO_3$ leftovers.

Fig. 4**c and 4d** show AFM and scanning electron microscopy images of the region of interest after reaction with $AgNO_3$. We see the formation of nanoparticles that selectively accumulate on the strained region and at the GaSe edge. Elemental analysis was carried out by energy dispersive X-ray analysis (EDX) (Fig. 4**e, f**, g, and h). These results show that GaSe catalytic activity was largely enhanced in the substrate-induced strained regions since EDX detected no Ag on the non-strained GaSe layers. It is worth noting that the distribution of Ag is not homogeneous. On the strained areas near the edge, the concentration of Ag is 4.4 %, while it is only 0.4 % far from the edge. This 10-fold increase in Ag deposition for the flake edges and the absence of Ag on non-strained regions show an emerging application in 2D materials engineering due to mechanical deformation, that is, straintronics [62]. Beyond providing a versatile substrate for electronic, morphological, and spectroscopic nanoscale characterization of 2D materials, the strong interaction makes it possible to investigate the strain in 3D structures by patterning HOPG.

The selective reaction of $AgNO_3$ with laser-irradiated GaSe enhances the photocatalytic properties, which are limited in unmodified GaSe [43]. After calculating dissociation and solvation energies during the cation exchange reaction, reported by Rivest *et al.* [63], we postulate that the reaction between $AgNO_3$ and GaSe is driven by cation exchange in the following way:

$$2Ag^{+} + GaSe \rightarrow Ag_2Se + Ga^{2+} \quad (2)$$

$GaSe \rightarrow Ga + Se$ dissociation energy: 207.44 kJ/mol; [64].

$Ag^{+} \rightarrow Ag$ desolvation energy: 350 kJ/mol; [65].

$2Ag + Se \rightarrow Ag_2Se$ association energy: −210 kJ/mol; [65].

$Ga \rightarrow Ga^{2+}$ solvation energy: −1678.97 kJ/mol, calculated as in the report by Marcus [66].

The total Gibbs energy for equation (2) is: $207.44 + 350 - 210 - 1678.97 = -1331.53$ kJ/mol. The negative value implies that the reaction is spontaneous at room temperature and thermodynamically favorable [67]. The Raman spectra of GaSe at different locations are shown in Fig. 4**i**. Crystalline GaSe has three main vibrational modes at 132, 212, and 307 cm^{-1}, shown in location 1. The Raman spectrum at location 2 shows three characteristic peaks, with one small peak rising at 230 cm^{-1}, corresponding to the Se-Se vibration mode in Ag_2Se [68]. In contrast to spot 2, the Raman spectrum at spot 1 shows a significant rise of peaks at 230 and 250 cm^{-1}, corresponding to the Se-Se vibration mode in Ag_2Se[68] and the E'(LO) mode activated by defects, respectively [51]. This also confirms the formation of Ag_2Se nanoparticles on GaSe strained regions. The possibility to drive chemical reactions using the most abundant energy source at our disposal is of fundamental importance. Therefore, we further investigated the photocatalytic activity of newly formed Ag-GaSe nanostructures using 4-nitrobenzenethiol (4-NBT) as a model molecular system for photocatalysis [69].

The conversion of 4-NBT to 4-aminobenzenethiol (4-ABT) and p,p′-dimercaptoazobenzene (DMAB) under laser irradiation has been studied intensively [70,71]. Raman spectroscopy is ideal for this investigation since we can simultaneously induce the chemical reaction and monitor the photocatalytic conversion thanks to the distinct vibrational modes between the reactant and products. 4-NBT has several prominent peaks at 1077, 1110, and 1340 cm^{-1}, contributing to in-plane C—H bending modes, and NO_2 mode, while the peak at 1575 cm^{-1} arises from the C—C stretching mode [72].

Our Raman spectroscopy results in Fig. 4**k** show that none of the 4-NBT, 4-ABT, or DMAB species were detected on flat non-strained GaSe (like point 3). This further confirms that no Ag was on the flat GaSe surface, but the substrate-induced strain made the GaSe wrinkles catalytically active as evidenced by the Raman spectra at points 1 and 2. The spectra in those regions match that of DMAB. We should also consider the intrinsic activity of steps in HOPG that have coordinatively unsaturated sites with a higher density of states. Even though these edges are underneath GaSe, their characteristics could enhance photocatalytic activity. Therefore, a control experiment was performed on bare HOPG, with no GaSe, to rule out contributions from HOPG steps reactivity. Our analysis shows that there was no detectable photocatalytic activity from HOPG steps confirming that the enhanced activity in this system is due to strained GaSe decorated with Ag NPs. Indeed, we discovered a new venue for a clean and versatile way to engineer defects on 2D materials by either exploiting graphite steps and natural defects or pre-patterning a HOPG substrate. After depositing the 2D material on a patterned HOPG the defects translocate to the 2D. These results show that the strong interaction between the 2D material and pre-existing defects in HOPG can be exploited in straintronics, giving rise to localized changes in reactivity, optical, and electronic properties.

In this work, we chose the mechanical transfer method because of its low cost, simplicity, speed, and versatility in investigating the intrinsic properties of 2D material. Moreover, transferring 2D materials onto substrate allows investigating any 2D materials regardless of their growth method, especially those not synthesized yet, such as naturally-occurring layered minerals. Also, we can transfer arbitrary 2D flakes onto steps of HOPG for strain engineering, which is demonstrated in this work and cannot be realized by directly growing them on a HOPG substrate. Nevertheless, the unique chemical and temperature stability of HOPG could also open the door for the direct growth of 2D materials with compatible methods such as electrochemistry and other chemical and physical growth techniques. This is indeed a perspective that we aim to explore next.

In summary, this work has several novelty points that were possible thanks to using HOPG as the substrate for 2D investigation. For example, it is the first time that: 1) the new 2D material zinc indium sulfide is investigated in its large-area layered single-crystal form; 2) the same substrate is used for all the nanoscale characterization methods we showed without any additional sample preparation steps, and the deposition from the bulk taking literally just a few seconds; 3) substrate-induced strain engineering is reported for the two-dimensional semiconductor GaSe activating its photocatalytic properties; 4) achieved visualization of single-layers without the optical interference of the conventional SiO_2/Si substrate; 5) evidence that 2D materials can become transparent to structural defects of the substrate underneath.

3. Conclusion

We comprehensively investigated the optical and electronic properties of several two-dimensional materials, including GaSe, MoS_2, $Zn_2In_2S_5$, talc, and h-BN (see Supporting information), using HOPG as a substrate. We demonstrated HOPG advantages for investigating 2D materials with various state-of-the-art nanoscale methods. The optical contrast of layered structures on HOPG with thickness ranging from single to few layers and its visibility on the graphite surface was elucidated. We performed a layer thickness *vs.* optical contrast evaluation for fast estimation of the thickness of 2D material on the HOPG substrate *via* optical contrast dependence with the layer number. Using KPFM and DFM, for the first time, we investigated electronic properties such as the work function and majority carrier type of a widely known 2D semiconductor GaSe and the novel two-dimensional material $Zn_2In_2S_5$. For the latter, we also demonstrated the influence of handmade and transferred defects on its work function, offering mechanical patterning and energy levels engineering possibilities. In addition, PL and Raman spectroscopy for MoS_2 was conducted to discuss intensity (PL) and peak position shifting (Raman) dependent on the number of layers showing no significant effects when using HOPG compared to the conventional Si/SiO_2. This could be done thanks to HOPG's Raman spectrum, which does not overlap with low-frequency Raman bands of 2D materials (usually lower than 600 cm^{-1}). The van der Waals nature of HOPG gave rise to a strong 2D material interaction that goes beyond the realm of van der Waals forces into the chemical range, opening new routes for 2D material engineering. Finally, the strong interaction and the multistep nature of the HOPG surface were exploited for strain engineering on GaSe for localization of photocatalytic properties enhancement by selective catalytic growth of Ag nanostructures from $AgNO_3$ on strained regions. The multifunctionality added by Ag nanostructures was further exploited in the photocatalytic 4-NBT conversion. We anticipate that these eye-opening demonstrations will motivate the active research community working on 2D materials to discover and manipulate new phenomena using an old but still unexplored substrate material as a platform.

4. Materials and methods

Natural solid crystals of MoS_2 were used for the preparation of flakes. GaSe crystal was grown by the Bridgman method. $Zn_2In_2S_5$ single crystal was synthesized by a chemical transport method. Synthetic hBN single crystals were acquired from HQ Graphene. Natural talc (steatite) single crystals were used to obtain thin talc layers. The mechanical exfoliation method was used to transfer all the flakes to the HOPG surface (except talc and h-BN). Talc and h-BN were transferred *via* the PDMS stamping method (**Figure. S1** in Supporting Information). Exfoliated nanolayers first have been observed by the optical microscope. Optical contrast between flakes and HOPG and the absence of light interference are the indicators of nanoscale flakes. Then, samples were scanned by the NTEGRA NT-MDT AFM system in contact topography mode to verify their thickness and measured by conductive modes SCM and KPFM. In SCM and KPFM, samples were scanned in intermittent contact mode (tapping-mode), and conductive NSG01/Pt cantilevers with force constant of 1.45–15.1 N/m. All AFM cantilevers were purchased from NT-MDT. Raman measurements on MoS_2 were acquired using the Horiba - LabRam Evolution setup. AFM topography images, including talc and h-BN, were obtained using an AIST-NT scanning probe microscope. **Silver deposition**: 10 μL of 1 mM $AgNO_3$ was dropped on the GaSe flake on HOPG. After 3 mins, $AgNO_3$ was sucked out, and the sample was washed to remove residual $AgNO_3$. Photocatalysis experiment: 4-NBT 10^{-3} M was prepared by mixing 7.75 mg in 25 mL distilled water and 25 mL ethanol. The sample was immersed in solution 4-NBT for 3 h; after that, the sample was washed with distilled water and measured in the Raman mode in the NTEGRA NT-MDT AFM system.

CRediT authorship contribution statement

Tuan-Hoang Tran: Conceptualization, Data curation, Formal analysis, Investigation, Methodology, Visualization, Writing – original draft. **Raul D. Rodriguez:** Supervision, Validation, Conceptualization, Data curation, Formal analysis, Methodology, Funding acquisition, Visualization. **Dmitry Cheshev:** Conceptualization, Data curation, Formal analysis, Investigation, Methodology, Visualization, Writing – original draft. **Nelson E. Villa:** Data curation, Formal analysis, Investigation, Methodology, Writing – original draft. **Muhammad Awais Aslam:** Data curation, Formal analysis, Investigation. **Jelena Pešić:** Data curation, Formal analysis. **Aleksandar Matković:** Data curation, Formal analysis, Validation, Funding acquisition. **Evgeniya Sheremet:** Supervision, Validation, Funding acquisition.

Declaration of Competing Interest

The authors declare that they have no known competing financial interests or personal relationships that could have appeared to influence the work reported in this paper.

Data availability

Data will be made available on request.

Acknowledgments

This work was funded by RFBR and FWF research project No. 19-52-14006. M.A.A. and A.M. acknowledge the support by the Austrian Science Fund (FWF Der Wissenschaftsfonds) through project I4323- N36. We are grateful to the Prof. Mekhman Yusubov and the Chemistry Research School at TPU for support with the acquisition of the AFM/Raman setup. Infrastructural support (Raman-TERS laboratory) by Montanuniversität Leoben is acknowledged. JP acknowledges the funding provided by the Institute of Physics Belgrade, through a grant from the Ministry of Education, Science and Technological Development of the Republic of Serbia. We are grateful to Prof. Bernardo R. A. Neves from the Federal University of Minas Gerais, Brasil, for kindly providing the natural talc (steatite) crystals. We thank Gennadiy Murastov for his assistance with AFM experiments.

Appendix A. Supplementary material

Supplementary data to this article can be found online at https://doi.org/10.1016/j.apsusc.2022.154585.

References

[1] M. Velický, P.S. Toth, Appl. Mater. Today 8 (2017) 68.

[2] H.S.N. Jayawardena, S.H. Liyanage, K. Rathnayake, U. Patel, M. Yan, Anal. Chem. 2021 (1889) 93.

[3] L. Zhang, H. Nan, X. Zhang, Q. Liang, A. Du, Z. Ni, X. Gu, K.K. Ostrikov, S. Xiao, Nat. Commun. 11 (2020) 5960.

[4] D.J. Late, B. Liu, H.S. Ramakrishna Matte, C.N.R. Rao, V.P. Dravid, Adv. Funct. Mater. 22 (2012) 1894.

[5] X.F. Fan, W.T. Zheng, V. Chihaia, Z.X. Shen, J.-L. Kuo, J. Phys. Condens. Matter 24 (2012), 305004.

[6] M. Lafkioti, B. Krauss, T. Lohmann, U. Zschieschang, H. Klauk, K.V. Klitzing, J. H. Smet, Nano Lett. 10 (2010) 1149.

[7] S.B. Desai, S.R. Madhvapathy, M. Amani, D. Kiriya, M. Hettick, M. Tosun, Y. Zhou, M. Dubey, J.W. Ager 3rd, D. Chrzan, A. Javey, Adv. Mater. 28 (2016) 4053.

[8] K.S. Novoselov, A. Mishchenko, A. Carvalho, A.H. Castro Neto, Science 353 (2016) aac9439.

[9] X. Gao, Y. Shen, Y. Ma, S. Wu, Z. Zhou, Comput. Mater. Sci. 170 (2019), 109200.

[10] K.D. Pham, N.N. Hieu, H.V. Phuc, I.A. Fedorov, C.A. Duque, B. Amin, C.V. Nguyen, Appl. Phys. Lett. 113 (2018), 171605.

[11] M. Kettner, C. Stumm, M. Schwarz, C. Schuschke, J. Libuda, Surf. Sci. 679 (2019) 64.

[12] J. Cryst, Growth 480 (2017) 13.

[13] Q. Li, M.A. Brown, J.C. Hemminger, R.M. Penner, Chem. Mater. 18 (2006) 3432.

[14] C. Herbig, C. Zhang, F. Mujid, S. Xie, Z. Pedramrazi, J. Park, M.F. Crommie, Nano Lett. 21 (2021) 2363.

[15] L. Meng, Y. Li, T.S. Liu, C. Zhu, Q.Y. Li, X. Chen, S. Zhang, X. Zhang, L. Bao, Y. Huang, F. Xu, R.S. Ruoff, Carbon 156 (2020) 24.

[16] R. Frisenda, E. Navarro-Moratalla, P. Gant, D. Pérez De Lara, P. Jarillo-Herrero, R. V. Gorbachev, A. Castellanos-Gomez, Chem. Soc. Rev. 47 (2018) 53.

[17] J.J. Schwartz, H.-J. Chuang, M.R. Rosenberger, S.V. Sivaram, K.M. McCreary, B. T. Jonker, A. Centrone, ACS Appl. Mater. Interfaces 11 (2019) 25578.

[18] K. Kato, F. Tanno, N. Umemura, Appl. Opt. 52 (2013) 2325.

[19] H. Li, J. Wu, X. Huang, G. Lu, J. Yang, X. Lu, Q. Xiong, H. Zhang, ACS Nano 7 (2013) 10344.

[20] F. Huang, J. Phys. Chem. C 123 (2019) 7440.

[21] J.M. Katzen, M. Velický, Y. Huang, S. Drakeley, W. Hendren, R.M. Bowman, Q. Cai, Y. Chen, L.H. Li, F. Huang, ACS Appl. Mater. Interfaces 10 (2018) 22520.

[22] X.-L. Li, W.-P. Han, J.-B. Wu, X.-F. Qiao, J. Zhang, P.-H. Tan, Adv. Funct. Mater. 27 (2017) 1604468.

[23] P. Gant, F. Ghasemi, D. Maeso, C. Munuera, E. López-Elvira, R. Frisenda, D.P. De Lara, G. Rubio-Bollinger, M. Garcia-Hernandez, A. Castellanos-Gomez, Beilstein J. Nanotechnol. 8 (2017) 2357.

[24] P. Blake, E.W. Hill, A.H. Castro Neto, K.S. Novoselov, D. Jiang, R. Yang, T.J. Booth, A.K. Geim, Appl. Phys. Lett. 91 (2007), 063124.

[25] P. Hlubina, J. Luňáček, D. Ciprian, R. Chlebus, Appl. Phys. B 92 (2008) 203.
[26] P. Hu, Z. Wen, L. Wang, P. Tan, K. Xiao, ACS Nano 6 (2012) 5988.
[27] M. Nonnenmacher, M.P. O'Boyle, H.K. Wickramasinghe, Appl. Phys. Lett. 58 (1991) 2921.
[28] E. Sheremet, P. Meszmer, T. Blaudeck, S. Hartmann, C. Wagner, B. Ma, S. Hermann, B. Wunderle, S.E. Schulz, M. Hietschold, R.D. Rodriguez, D.R.T. Zahn, Phys. Status Solidi 216 (2019) 1900106.
[29] A. Matković, A. Petritz, G. Schider, M. Krammer, M. Kratzer, E. Karner-Petritz, A. Fian, H. Gold, M. Gärtner, A. Terfort, C. Teichert, E. Zojer, K. Zojer, B. Stadlober, Adv. Electron. Mater. 6 (2020) 2000110.
[30] W. Melitz, J. Shen, A.C. Kummel, S. Lee, Surf. Sci. Rep. 66 (2011) 1.
[31] L. Karvonen, A. Säynätjoki, S. Mehravar, R.D. Rodriguez, S. Hartmann, D.R. T. Zahn, S. Honkanen, R.A. Norwood, N. Peyghambarian, K. Kieu, H. Lipsanen, J. Riikonen, Sci. Rep. (2015) 5, https://doi.org/10.1038/srep10334.
[32] Z. B. Aziza, Z. Ben Aziza, D. Pierucci, H. Henck, M. G. Silly, C. David, M. Yoon, F. Sirotti, K. Xiao, M. Eddrief, J.-C. Girard, A. Ouerghi, Phys. Rev. B **2017**, 96, DOI 10.1103/physrevb.96.035407.
[33] M. Rahaman, R.D. Rodriguez, M. Monecke, S.A. Lopez-Rivera, D.R.T. Zahn, Semicond. Sci. Technol. 32 (2017), 105004.
[34] T.-H. Tran, R.D. Rodriguez, M. Salerno, A. Matković, C. Teichert, E. Sheremet, Carbon 176 (2021) 431.
[35] S.K. Chong, F. Long, G. Wang, Y.-C. Lin, S. Bhandari, R. Shahbazian-Yassar, K. Suenaga, R. Pandey, Y.K. Yap, ACS Appl. Nano Mater. 1 (2018) 3293.
[36] Z.I. Alferov, Russ. Chem. Rev. 82 (2013) 587.
[37] Y.Y. Illarionov, T. Knobloch, M. Jech, M. Lanza, D. Akinwande, M.I. Vexler, T. Mueller, M.C. Lemme, G. Fiori, F. Schwierz, T. Grasser, Nat. Commun. 11 (2020) 3385.
[38] J. Zhang, W. Lu, Y.S. Li, J. Cai, L. Chen, Acc. Chem. Res. 48 (2015) 1788.
[39] W. Lu, J. Zhang, Y.S. Li, Q. Chen, X. Wang, A. Hassanien, L. Chen, J. Phys. Chem. C 116 (2012) 7158.
[40] Y. Kang, D. Jeon, T. Kim, J. Phys. Chem. C 124 (2020) 18316.
[41] Z.B. Aziza, Z. Ben Aziza, H. Henck, D. Pierucci, M.G. Silly, E. Lhuillier, G. Patriarche, F. Sirotti, M. Eddrief, A. Ouerghi, ACS Nano 10 (2016) 9679.
[42] M. Zhong, Q. Xia, L. Pan, Y. Liu, Y. Chen, H.-X. Deng, J. Li, Z. Wei, Adv. Funct. Mater. 28 (2018) 1870312.
[43] D. Cheshev, R.D. Rodriguez, A. Matković, A. Ruban, J.-J. Chen, E. Sheremet, ACS Omega 5 (2020) 10183.
[44] R. Bel Hadj Tahar, T. Ban, Y. Ohya, Y. Takahashi, J. Appl. Phys. **1998**, 83, 2631.
[45] E. Mercado, Y. Zhou, Y. Xie, Q. Zhao, H. Cai, B. Chen, W. Jie, S. Tongay, T. Wang, M. Kuball, ACS Omega 4 (2019) 18002.
[46] H. Wang, Y. Sun, Y. Wu, W. Tu, S. Wu, X. Yuan, G. Zeng, Z.J. Xu, S. Li, J.W. Chew, Appl. Catal. B 245 (2019) 290.
[47] H. Zhang, S. Xie, J. Hu, X. Wu, Q. Zhang, J. Cheng, Y. Wang, Chem. Commun. 56 (2020) 1776.
[48] S. Yang, Y. Chen, C. Jiang, InfoMat 3 (2021) 397.
[49] B. Vasić, A. Matković, U. Ralević, M. Belić, R. Gajić, Carbon 120 (2017) 137.
[50] Z. Li, Y. Wang, A. Kozbial, G. Shenoy, F. Zhou, R. McGinley, P. Ireland, B. Morganstein, A. Kunkel, S.P. Surwade, L. Li, H. Liu, Nat. Mater. 12 (2013) 925.
[51] R.D. Rodriguez, S. Müller, E. Sheremet, D.R.T. Zahn, A. Villabona, S.A. Lopez-Rivera, P. Tonndorf, S.M. de Vasconcellos, R. Bratschitsch, J. Vacuum Sci. Technol. B Nanotechnol. Microelectron. Mater. Process. Measurem. Phenomena 32 (2014) 04E106.
[52] A. Anshul, M. Kumar, A. Raj, Optik 212 (2020), 164749.
[53] T.P. Darlington, C. Carmesin, M. Florian, E. Yanev, O. Ajayi, J. Ardelean, D. A. Rhodes, A. Ghiotto, A. Krayev, K. Watanabe, T. Taniguchi, J.W. Kysar, A. N. Pasupathy, J.C. Hone, F. Jahnke, N.J. Borys, P.J. Schuck, Nat. Nanotechnol. 15 (2020) 854.
[54] A.V. Tyurnina, D.A. Bandurin, E. Khestanova, V.G. Kravets, M. Koperski, F. Guinea, A.N. Grigorenko, A.K. Geim, I.V. Grigorieva, ACS Photonics 6 (2019) 516.
[55] A. Splendiani, L. Sun, Y. Zhang, T. Li, J. Kim, C.-Y. Chim, G. Galli, F. Wang, Nano Lett. 10 (2010) 1271.
[56] H. Li, Q. Zhang, C.C.R. Yap, B.K. Tay, T.H.T. Edwin, A. Olivier, D. Baillargeat, Adv. Funct. Mater. 22 (2012) 1385.
[57] G. Eda, H. Yamaguchi, D. Voiry, T. Fujita, M. Chen, M. Chhowalla, Nano Lett. 11 (2011) 5111.
[58] A. Matković, L. Ludescher, O. E. Peil, A. Sharma, K.-P. Gradwohl, M. Kratzer, M. Zimmermann, J. Genser, D. Knez, E. Fisslthaler, C. Gammer, A. Lugstein, R. J. Bakker, L. Romaner, D. R. T. Zahn, F. Hofer, G. Salvan, J. G. Raith, C. Teichert, *npj 2D Materials and Applications* **2021**, *5*, DOI 10.1038/s41699-021-00276-3.
[59] S. Dou, X. Wang, S. Wang, Small Methods 3 (2019) 1800211.
[60] Z. Dai, L. Liu, Z. Zhang, Adv. Mater. 31 (2019) 1970322.
[61] Y. Wu, L. Wang, H. Li, Q. Dong, S. Liu, Strain of 2D materials via substrate engineering, Chin. Chem. Lett. 33 (2022) 153–162.
[62] F. Miao, S.-J. Liang, B. Cheng, *npj quantum mater.* **2021**, *6*, DOI 10.1038/s41535-021-00360-3.
[63] J.B. Rivest, P.K. Jain, Chem. Soc. Rev. 42 (2013) 89.
[64] M. Ider, R. Pankajavalli, W. Zhuang, J.Y. Shen, T.J. Anderson, ECS J. Solid State Sci. Technol. 4 (2015) Q51.
[65] N. Chen, M.R. Scimeca, S.J. Paul, S.B. Hafiz, Z. Yang, X. Liu, F. Yang, D.-K. Ko, A. Sahu, Nanoscale Adv. 2 (2020) 368.
[66] Y. Marcus, J. Chem. Soc., Faraday Trans. 87 (1991) 2995.
[67] H. Jin, C. Guo, X. Liu, J. Liu, A. Vasileff, Y. Jiao, Y. Zheng, S.-Z. Qiao, Chem. Rev. 118 (2018) 6337.
[68] M. Pandiaraman, N. Soundararajan, J. Theor. Appl. Phys. 6 (2012) 7.
[69] J.-L. Yang, H.-J. Wang, H. Zhang, Z.-Q. Tian, J.-F. Li, Cell Rep. Phys. Sci. 1 (2020), 100184.
[70] Y. Fang, Y. Li, H. Xu, M. Sun, P. M. Champion, L. D. Ziegler, **2010**, DOI 10.1063/1.3482306.
[71] A.A. Golubev, B.N. Khlebtsov, R.D. Rodriguez, Y. Chen, D.R.T. Zahn, J. Phys. Chem. C 122 (2018) 5657.
[72] K. Kim, I. Lee, S.J. Lee, Chem. Phys. Lett. 377 (2003) 201.